

*Review*

# Gamma Ray Pulsars and Opportunities for the MACE Telescope

Atul Pathania <sup>1</sup>, Krishna Kumar Singh <sup>1,2,\*</sup> and Kuldeep Kumar Yadav <sup>1,2</sup>

<sup>1</sup> Astrophysical Sciences Division, Bhabha Atomic Research Centre, Mumbai 400085, India; apathania@barc.gov.in (A.P.); kkyadav@barc.gov.in (K.K.Y.)

<sup>2</sup> Homi Bhabha National Institute, Anushakti Nagar, Mumbai 400094, India

\* Correspondence: kksastro@barc.gov.in

**Abstract:** Rapidly rotating neutron stars with very strong surface magnetic fields are observed to emit pulsed emission in the whole range of electromagnetic spectrum from radio to high-energy gamma rays. These so-called pulsars are known for their exceptional rotational stability. The radio emission from pulsars is generally believed to be powered by the rotational energy of neutron stars. More than 3000 pulsars have been currently known from radio observations; however, only about 10% are observed in the high-energy gamma ray band. The *Fermi*-LAT observations in the energy range above 100 MeV have discovered more than 300 pulsars. However, the origin of high-energy non-thermal radiation from pulsars is not completely understood and remains an active area of research. In this contribution, we report a summary of observational features of the gamma ray pulsars and briefly discuss observability for the MACE gamma ray telescope, which has just started its regular science operation at Hanle in India. Six gamma ray pulsars, other than the well-known Crab and Geminga, are identified as probable candidates for MACE observations.

**Keywords:** pulsars; gamma rays; MACE telescope



**Citation:** Pathania, A.; Singh, K.K.; Yadav, K.K. Gamma Ray Pulsars and Opportunities for the MACE Telescope. *Galaxies* **2023**, *11*, 91. <https://doi.org/10.3390/galaxies11040091>

Academic Editor: Bidzina Kapanadze

Received: 26 June 2023

Revised: 12 August 2023

Accepted: 16 August 2023

Published: 17 August 2023



**Copyright:** © 2023 by the authors. Licensee MDPI, Basel, Switzerland. This article is an open access article distributed under the terms and conditions of the Creative Commons Attribution (CC BY) license (<https://creativecommons.org/licenses/by/4.0/>).

## 1. Introduction

A high-energy phenomenon, the so-called supernova explosion, takes place at the end of stellar evolution cycle of massive stars [1]. A huge amount of energy, released by the gravitationally collapsing stellar core, produces shocks that eject the outer layers of the progenitor star. This leads to the formation of relativistic compact objects such as a neutron star or a black hole with a very high matter density [2]. The mass of neutron stars is in the range  $1\text{--}3 M_{\odot}$  and the radius is around 10 km [3,4]. Such objects reach extreme physical conditions of density, temperature, pressure, strong surface magnetic fields and rapid rotation. Generally, neutron stars are formed after the core collapse of stars with initial masses in the range  $8\text{--}20 M_{\odot}$  and the corresponding supernova explosion asymmetrically ejects the matter at a very high velocity of  $\sim 10^9 \text{ cm s}^{-1}$  [5,6]. It is hypothesized that asymmetric ejection of matter may impart natal kicks to the neutron star due to conservation of momentum, leading to high neutron star velocity. Consequently, the resulting kick force, unless it is exerted exactly head-on at the center of star, and conservation of the progenitor angular momentum can cause the rotation of neutron star. However, the exact physical processes which kick the neutron star initially at birth and cause its rotation have not been clearly understood and is still under debate [7–9]. Rapidly spinning/rotating neutron stars with strong surface magnetic field ( $10^8\text{--}10^{12} \text{ G}$ ) and surrounded by a magnetosphere filled with plasma are referred to as *pulsars* [10,11]. The strength and structure of a magnetic field play a significant role in describing the observational properties and ages of pulsars. Numerical simulations suggest that isolated pulsars (spherical neutron star with dipole magnetic field) follow the *spin-down law* of the form [12]

$$P \dot{P} = \frac{8\pi^2 \mu^2}{3Ic^3} (1 + \sin^2 \alpha) \quad (1)$$

where  $P$  is spin period of the pulsar,  $\dot{P}$  is time-derivative of  $P$  or spin-down rate,  $\mu$  and  $I$  are, respectively, the magnetic dipole moment and moment of inertia of the neutron star,  $\alpha$  is the angle between magnetic and rotation/spin axes and  $c$  is speed of light in vacuum. Angle  $\alpha$  is also referred to as the *magnetic angle* or the *magnetic obliquity* of the neutron star. The values of  $\alpha$  close to  $0^\circ$  and  $90^\circ$  correspond to the aligned and orthogonal pulsars, respectively. The field lines of a strong magnetic field of a pulsar are anchored to the outer crust of the neutron star. This results in the rotation axis and frequency of rotation of the surface magnetic field being same as the pulsar rotation axis and its spin frequency, respectively. A strong electric potential is produced at the magnetic poles due to the co-rotation of the magnetic field lines near the surface and outer crust of the neutron star. This electric potential generates a powerful current of charged particles traveling along the field lines in the magnetosphere [13,14]. The charged particles moving along the magnetic field lines create a radiation cone that is centered on the magnetic axis. Since the magnetic axis does not coincide with the spin/rotation axis, a series of periodic pulses are detected due to the rotation of a neutron star if the radiation cone sweeps past our line of sight. Therefore, the pulsars are considered as an astronomical lighthouse. The pulsed radiation measured from pulsars spans over the entire electromagnetic spectrum ranging from radio to high-energy gamma rays and is very precisely characterized by their spin period ( $P$ ).

Historically, the first pulsar CP1919 (CP: Cambridge Pulsar) or *PSR B1919+21* with  $P = 1.34$  s was discovered by Jocelyn Bell, Antony Hewish and their colleagues in 1967 at the Cambridge University using an array of dipoles tuned to 81.5 MHz radio frequency. However, the official announcement was made in the 24 February 1968 edition of the prestigious *Nature* journal [10] and the Nobel Prize in Physics was awarded to Antony Hewish in 1974 for the discovery of pulsars. This breakthrough result was interpreted as either the rotation of a neutron star or the radial pulsations of a white dwarf. Subsequently, about 30 pulsars were detected using radio observations in a span of two years and a sudden decrease in the pulsar spin period (pulsar glitch) by about three parts in a million was also discovered in 1969 [15,16]. The discovery of first binary pulsar PSR B1913+16 by Russell Hulse and Joe Taylor in 1974 provided the first accurate measurement of neutron star mass and allowed for the measurement of the orbital decay, providing evidence for emission of gravitational waves [17]. The next important discovery of a millisecond pulsar PSR B1937+214 with  $P = 1.558$  ms resolved the puzzle of extremely steep radio spectrum of pulsars in 1982 [18]. A unique binary radio pulsar PSR J0737–3039A/B with  $P = 22$  ms and an orbital period of 2.4 h was discovered in 2003 [19]. This binary system comprises two neutron stars of different ages, and their orbit can be viewed exactly edge-on. The discovery of this eclipsing binary pulsar system has been hailed as a milestone both in observational search as well as exploring the fundamental physics. Over the past 50 years, pulsar astronomy has made very impressive progress as the number of known pulsars in our Milky Way Galaxy has rapidly grown to more than 3000, including isolated and binary pulsars with diverse characteristics over the entire electromagnetic spectrum<sup>1</sup> [20]. The distribution of latitudes and longitudes of the known pulsar population in the Milky Way Galaxy are shown in Figure 1. It is evident that the Galactic latitude of most of the pulsars is close to zero. This suggests that the Galactic plane is populated with the pulsars. The Galactic longitude distribution peaking at  $0^\circ$  or  $360^\circ$  implies that the pulsar population is concentrated towards the Galactic center in the inner and outer Galactic planes. This can be attributed to the geometry and the sky coverage by radio surveys. A vast majority of these pulsars are observed in the radio waveband, a small fraction in the high-energy gamma ray band, and dozens of pulsars in X-ray/optical bands [20]. However, only four pulsars are detected in the very-high-energy region [21].

In a certain configuration of binary systems comprising a neutron star and a main sequence companion star, the size of the companion star increases significantly as it ages into a red or blue giant. This leads to the Roche lobe overflow, where mass transfer takes place from the companion star to the neutron star. The transfer of angular momentum along with the mass transfer causes the neutron star to spin up while remaining in the

stable orbit with its companion star. The accretion process continues until the neutron star attains fast spinning. At this point, the emission of electromagnetic radiation from pulsar resumes and the accretion disk is blown away, leaving a rapidly rotating pulsar in the binary system. The pulsed emission is generated through the channeling of accreted matter with the magnetic field of the neutron star. The matter is accumulated on the magnetic poles of the neutron star. This leads to the creation of hot-spots on the neutron star surface. These hot-spots occur brighter at X-ray energies due to the rotation of the neutron star around its axis, and therefore, X-ray pulsations are produced. Thus, a neutron star sometimes makes the transition into a pulsar through the accretion of matter in a so-called recycling process [22,23]. Such a recycling scenario is strongly supported by observations of accreting X-ray binary pulsars [24,25].

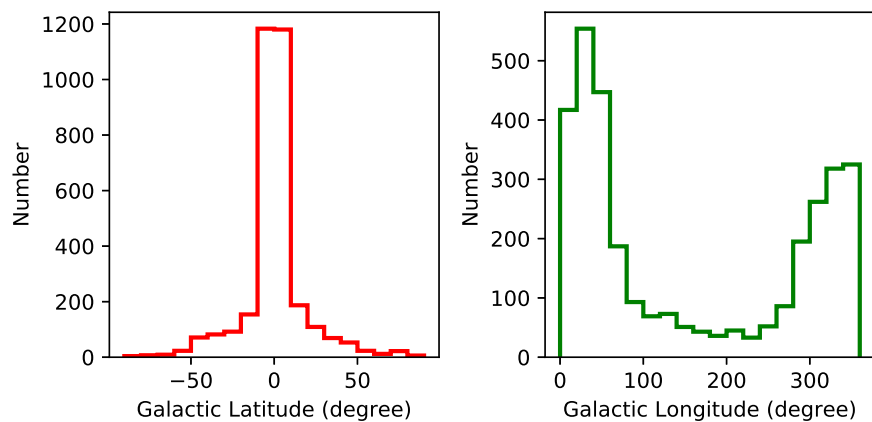


**Figure 1.** Distribution of Galactic latitude and longitude of more than 3000 known pulsars.

On the basis of plausible physical processes involved in the emission of radiation, pulsars are classified into three types: *rotation-powered pulsars*, *accretion-powered pulsars* and *internal-energy-powered pulsars* [26]. In the rotation-powered pulsars, the emission of electromagnetic radiation is attributed to the loss of rotational kinetic energy of the neutron star due to magnetic braking. This group of pulsars is further classified as classical radio pulsars, millisecond radio pulsars and mildly recycled pulsars, depending upon the spin period ( $P$ ) and strength of the neutron star surface magnetic field ( $B_p$ ). The classical radio pulsars exhibit  $P \sim 1$  s and  $B_p \sim 10^{11}$ – $10^{14}$  G, whereas millisecond radio pulsars and mildly recycled pulsars have  $P \leq 20$  ms,  $B_p \leq 10^{10}$  G and  $P \sim 20$ – $100$  ms,  $B_p \leq 10^{11}$  G, respectively [27]. In the accretion-powered pulsars, material accretion on to the neutron star is responsible for the emission of energetic radiation. These pulsars are generally observed as a binary system consisting of a neutron star as a compact object and a main sequence companion star as a donor star. Depending on the mass of companion star, the accretion-powered pulsars are classified as low-mass X-ray binary or high-mass X-ray binary. In low-mass X-ray binary pulsars, the surface magnetic field of the neutron star is weak ( $B_p \leq 10^{11}$  G) due to the extended phase of accretion [28]. Thermonuclear X-ray burst, accretion-powered millisecond pulsations, kHz quasi-periodic oscillations, broad relativistic iron lines and quiescent emission are the main physical processes taking place in low-mass X-ray binary systems. On the other hand, high-mass X-ray binaries harbor neutron stars with a relatively strong surface magnetic field  $B_p \sim 10^{12}$  G. These objects are mostly observed in X-rays with hard spectrum [29]. The X-ray emission from such pulsars has the signatures of Comptonization due to the interaction of accretion plasma with the magnetic field of the neutron star and the presence of Cyclotron broad absorption lines, referred to as the Cyclotron Resonance Scattering Feature. Finally, the internal-energy-powered pulsars form a new class where the exact physical mechanism for the emission of radiation is not known. However, it is assumed that the internal energy reservoir in the form of strong magnetic field decay or residual cooling powers the observed emission [30].

Magnetars, soft gamma ray repeaters and anomalous X-ray pulsars are believed to be members of the group of internal-energy-powered pulsars [31]. Another classification of known pulsars is also proposed on the basis of their measured spin period. According to this classification, pulsars are of two types: *millisecond pulsars* (MSPs) and *normal pulsars* (NPs). MSPs exhibit  $P \leq 20$  ms and  $B_p \sim 10^8\text{--}10^{10}$  G, whereas NPs have  $P > 20$  ms and  $B_p \sim 10^{10}\text{--}10^{12}$  G. It is believed that MSPs in binary systems are recycled pulsars [32].

The launch of a large area telescope onboard the *Fermi* satellite in 2008 has led to the discovery of a number of gamma ray pulsars. However, only a few of them have been detected so far by the ground-based gamma ray instruments. In this paper, we mainly focus on the gamma ray pulsars and explore the potential of recently commissioned MACE (Major Atmospheric Cherenkov Experiment) telescope to detect the pulsed emission above 20 GeV. The remainder of this paper is organized as follows. In Section 2, we discuss the empirical properties of pulsars. A brief review of gamma ray pulsars is given in Section 3. In Section 4, we describe the salient features of the MACE telescope. We then discuss the results from the feasibility studies for pulsar observations with MACE in Section 5. Finally, we summarize our research in Section 6.

## 2. Pulsar Characteristics

A complete understanding of the underlying physical processes involved in the pulsed electromagnetic emission and geometry of the emission region is far from complete. Soon after the pulsar discovery, it was argued that, on the basis of observed features, the powerhouse of a pulsar is a fast spinning/rotating neutron star with a strong surface magnetic field [11]. The periodic nature of pulsar emission observed on Earth, with incredible timing accuracy comparable to the atomic clock, is understood in the framework of a *lighthouse* model, as the magnetic axis of a rotating neutron star sweeps across the line of sight of an observer. The emission mechanism is linked to the magnetic-field-affected co-rotating plasma in the pulsar magnetosphere with less understood structure and dynamics. It is still not clear whether the emission region is located out in the magnetosphere or close to the neutron star [33,34].

The spin-down law, given by Equation (1), is generally valid for any moment in the lifetime of the pulsars. Moreover, among the three parameters  $I$ ,  $\mu$  and  $\alpha$ , at least two are expected to change for a real pulsar. Therefore,  $B_p$  suffers a slow decay due to the Ohmic dissipation of electric currents in the neutron star crust [35]. The time evolution of the obliquity angle  $\alpha$  is given by

$$\frac{d\alpha}{dt} \propto \frac{B_p^2}{P^2} \sin(\alpha)\cos(\alpha) \quad (2)$$

Measurements from radio observations suggest that  $\alpha$  evolves on a timescale of  $10^7$  years [36]. This can lead to a situation where  $\alpha$  becomes zero and the magnetic axis of an isolated pulsar eventually aligns with its rotation axis on a timescale of  $P/\dot{P}$ . Sudden small changes in the rotation velocity of pulsars, generally referred to as pulsar glitches, are attributed to the transfer of angular momentum between the crust and another component of the neutron star [37]. The pulsar period  $P$  also changes continuously for the rotation-powered pulsars due to the loss of kinetic energy. Therefore, most of the pulsars slow down over the time despite their  $P$  being very stable, and the slow-down rate is given by  $\dot{P}$ . The parameters such as  $P$ ,  $\dot{P}$  and higher order time-derivatives of  $P$  are determined from the pulse time-of-arrival measurements over long intervals, ranging from hours to decades [38]. The precision in the measurement of the pulse time-of-arrival critically decides the amount of useful information that can be extracted for a pulsar through observations. The measured pulse time-of-arrival by a telescope on Earth corresponds to a non-inertial frame of reference measurement. Therefore, pulse time-of-arrivals are first translated to an inertial reference frame, normally the solar-system barycenter (an appropriate inertial reference frame), to remove the effects of Earth's rotational and orbital motion. A barycentric pulse arrival time is estimated for individual time-of-arrival on the basis of a model for the intrin-

sic properties of the pulsar including its astrometric, rotational and propagation effects in interstellar medium and other parameters. The difference between estimated and observed pulse arrival times is referred to as the timing *residual* and its study is very important for all pulsar timing measurements.

From the long-term pulsar timing measurements, the slow-down rate is derived as

$$\dot{P} = \frac{dP}{dt} = -\frac{1}{v^2} \frac{dv}{dt} \quad (3)$$

where  $v = 1/P$  is the pulse frequency or spin frequency of the pulsar. The intrinsic rotation of an isolated pulsar can be expressed by the Taylor-series expansion of  $v$  or  $P$  about a reference time  $t_0$  as [38]

$$v(T) = v_0 + \frac{dv_0}{dt}(T - t_0) + \frac{d^2v_0}{dt^2} \frac{(T - t_0)^2}{2} + \dots \quad (4)$$

or

$$P(T) = P_0 + \frac{dP_0}{dt}(T - t_0) + \frac{d^2P_0}{dt^2} \frac{(T - t_0)^2}{2} + \dots \quad (5)$$

where  $T$  is the pulsar proper time and  $v_0 = 1/P_0$  is the initial spin frequency at reference epoch  $t_0$ . The number of rotations completed by the neutron star from  $t_0$  is known as the pulsar phase ( $\phi$ ). The fractional part of  $\phi$  at a given epoch carries the information on orientation of the pulsar at that time. Pulses with same fraction of  $\phi$  are measured when pulsar orientation is aligned with the observer. Distribution of  $\phi$  attributed to each event recorded by a detector/telescope is known as the pulsar phase diagram or phasogram. This describes the pulsar rotation model in a reference frame co-moving with the pulsar or pulsar-ephemeris, which takes into account the changes in spin frequency with time due to the rotational energy loss. The pulsar spin-down contributes to the time-derivatives of  $v_0$  or  $P_0$ . From Equation (4), pulse number  $N$  can be written as [39]

$$N = N_0 + v_0(T - t_0) + \frac{1}{2} \frac{dv_0}{dt}(T - t_0)^2 + \frac{1}{6} \frac{d^2v_0}{dt^2}(T - t_0)^3 + \dots \quad (6)$$

where  $N_0$  is the number of pulses at  $t_0$ . The pulsar proper time  $T$  corresponds to its time at the solar-system barycenter of infinite frequency up to a constant and is expressed as [39]

$$T = t_t + t_c - \frac{D \times DM}{f^2} + \Delta_R + \Delta_S + \Delta_E \quad (7)$$

where  $t_t$  is pulse arrival time at telescope,  $t_c$  is relative time correction,  $(D \times DM/f^2)$  is dispersion correction,  $f$  is observation frequency,  $\Delta_R$  is delay due to Earth-motion around Sun,  $\Delta_S$  is the Shapiro delay due to space-time curvature, and  $\Delta_E$  is the Einstein delay. For a pulsar in binary system, extra time delays caused by the orbital motion of neutron star and gravitational field of the companion star are also included in  $T$ .

The distribution of  $\dot{P}$  versus  $P$  or  $P - \dot{P}$  diagram is used to identify the underlying physical process in the distinct group of pulsars [40]. For rotation-powered pulsars (i.e., NPs), values of  $P$  (0.3–3 s) and  $\dot{P}$  ( $\sim 10^{-15}$  s s $^{-1}$ ) are measured with high accuracy through the pulsar-timing measurements. For MSPs (mostly observed in binary systems),  $P$  is mostly less than 20 ms and  $\dot{P}$  ranges from  $10^{-18}$  s s $^{-1}$  to  $10^{-22}$  s s $^{-1}$ . The smaller values of  $\dot{P}$  for MSPs imply that their  $P$  is more stable than that of NPs on a longer timescale. The knowledge of  $P$  and  $\dot{P}$  is also used to estimate the magnetic field at the pulsar surface as [41]

$$B_p \approx 10^{12} \sqrt{\left(\frac{P}{1 \text{ s}}\right) \left(\frac{\dot{P}}{10^{-15} \text{ s s}^{-1}}\right)} \text{ G} \quad (8)$$

assuming a magnetic-dipole field structure. However, the actual  $B_p$  could be much stronger due to the presence of higher-order magnetic poles at the neutron star surface. The spin-

down history of an isolated pulsar can be captured by its  $P$  and  $\dot{P}$ . If the initial spin period  $P_0$  is much less than  $P$ , (Equation (5)), we have the *characteristic age* of pulsar given by [35]

$$\tau_{ch} = \frac{P}{2\dot{P}} \quad (9)$$

This corresponds to the time since the pulse period was zero and is used to estimate the true pulsar age ( $\tau_p$ ). A fiducial line (corresponding to the maximum accelerating potential) in the  $P - \dot{P}$  diagram, below which pulsar activity is considered to vanish, is referred to as the death line. A simplified view of pulsars suggests that the evolution of radio pulsars proceeds along the line of constant magnetic field and descends towards the death line in the  $P - \dot{P}$  diagram. It is theorized that, after crossing the death line, a pulsar becomes radio quiet; however, many pulsars are seen behind the death line. The true age of a rotation-powered pulsar is expressed as

$$\tau_p = \frac{2\tau_{ch}}{n-1} - \tau_0 \quad (10)$$

where  $\tau_0$  is the initial spin-down timescale and  $n$  is the *braking index*, which describes the secular spin down of pulsar. The braking index is defined as [42]

$$n = \frac{\nu \ddot{\nu}}{\dot{\nu}^2} = 2 - \frac{P \ddot{P}}{\dot{P}^2} \quad (11)$$

It is a characteristic tool to probe the magnetic field evolution.  $n = 3$  and 5 correspond to the braking due to the magnetic-dipole and gravitational wave emission, respectively. Braking by pulsar winds, which deform the magnetosphere, is characterized by the value of  $n$  ranging from 1.0 to 3.0. It is also used to describe the spin-down of a neutron star or pulsar using the torque equations as

$$\dot{\nu} = -K\nu^n \quad (12)$$

where  $K$  is a proportionality constant related to the energy loss mechanism of pulsar [43]. In case of a rotating magnetic dipole approximation, the spin-down luminosity ( $L_{sd}$ ) of pulsar is given by the rotation energy loss of the neutron star, i.e.,

$$L_{sd} = -\frac{d}{dt}E_{rot} = 4\pi^2 I \dot{P} P^{-3} \quad (13)$$

where  $E_{rot}$  is the rotational kinetic energy of neutron star and  $I$  is its moment of inertia [4]. This expression can be further simplified as

$$L_{sd} = \frac{4\pi^2 I}{P_0^2(n-1)\tau_0} \left(1 + \frac{\tau_p}{\tau_0}\right)^{-\frac{(n+1)}{(n-1)}} \quad (14)$$

and

$$\tau_0 = \frac{3c^3 I P_0^2}{4\pi^2 B_p^2 R^6} \quad (15)$$

where  $R$  is the radius of neutron star. For magnetic dipole braking ( $n = 3$ ), Equation (14) simply reduces to

$$L_{sd} \approx 1.1 \times 10^{34} \left(\frac{\tau_p}{10^6 \text{yr}}\right)^{-2} \text{erg s}^{-1} \quad (16)$$

This suggests that the braking timescale, over which the loss of rotational energy of the neutron star will slow down the pulsar spin, is  $\sim 10^6$  years. The luminosity ( $L_{sd}$ ) depends on  $B_p^2$  for both MSPs as well as NPs and, for a given  $B_p$ , MSPs are more luminous than NPs [41].

Thermal emission from the surface of the neutron star can be distinguished from the non-thermal emission arising from the pulsar magnetosphere in the X-ray band. Due to the strong gravitational field of the neutron star, general relativistic effects should be invoked in the interpretation of the observed X-ray luminosity of a pulsar [44]. The apparent bolometric thermal luminosity measured by a distant observer is given by

$$L_{obs}^{th} = L^{th}(1 + z_b)^{-2} \quad (17)$$

where  $L^{th}$  is the thermal luminosity emitted from the surface of the neutron star and  $z_b$  is the surface gravitational redshift. The apparent radii of neutron star is

$$R_{obs} = R(1 + z_b) \quad (18)$$

and the atmosphere redshifted effective temperature is

$$T_{obs} = \frac{T}{1 + z_b} \quad (19)$$

For a canonical neutron star,  $R = 10$  km,  $M = 1.4M_{\odot}$  and  $z_b \approx 0.15$ , the general relativistic effects may be important because the distantly observed thermal luminosity will be larger than the intrinsic luminosity by a factor of 1.32 or 32% higher.

### 3. Gamma Ray Pulsars

The first gamma ray pulsation at energies above 50 MeV was detected from the Crab pulsar (NP 0532) in 1971 by a detector consisting of a multiplate spark chamber in a balloon-borne experiment [45]. These gamma ray pulsations were observed at the radio period ( $P \approx 33$  ms) of the source. The launch of the *Small Astronomy Satellite* (SAS-2) in 1972 confirmed the pulsed gamma ray emission from the Crab and Vela pulsars [46,47]. The COS-B satellite, launched in 1975, confirmed and significantly improved the measurements of SAS-2 and also discovered a population of twenty unidentified gamma ray sources in the Milky Way Galaxy [48]. Both SAS-2 and COS-B detected pulsed gamma ray signal at low significance level from the known radio pulsars. The number of radio pulsars increased rapidly after their first discovery, but Crab and Vela remained the only known gamma ray pulsars for more than two decades after their first detection. Subsequently, the EGRET (Energetic Gamma Ray Experiment Telescope), onboard the Compton Gamma Ray Observatory, was launched in 1991 to search for more gamma ray pulsars apart from exploring the high-energy Universe. It detected a total of six gamma ray pulsars (Crab, B1509-58, Vela, B1706-44, B1951+32, Geminga, and B1055-52) and a few plausible candidates during its operation. Discovery of Geminga as a radio-quiet gamma ray pulsar was an important finding of EGRET, as it turned to be the prototype of young gamma ray pulsars [49–51]. Finally, the Large Area Telescope (LAT), onboard the *Fermi* satellite, has been able to discover about 340 gamma ray pulsars at energies above 100 MeV in a time span of approximately 15 years since its launch in 2008 [52]. It has not only confirmed the existence of radio-quiet gamma ray pulsars and MSPs, but has also established pulsars as dominant high-energy gamma ray sources in the Universe.

#### 3.1. Fermi-LAT Pulsars

Until 2008, pulsed gamma ray emission was mainly detected from pulsars that were initially observed in lower energy bands. Therefore, discovery and identification of new gamma ray sources was the main science goal of the *Fermi*-LAT [53]. Due to its large field of view of  $\sim 2.4$  sr, the *Fermi*-LAT completes continuous mapping of whole sky in about 3 h in survey mode. Therefore, observations of a few weeks to a few months are sufficient to build an average pulse profile for confirming a gamma ray source as a pulsar. The photon collection by the *Fermi*-LAT, with an accuracy better than 1  $\mu$ s, helps in the detection of even rapid pulsations from millisecond pulsars. The first *Fermi*-LAT pulsar catalog (1PC) containing 46 high-confidence pulsed detections in the energy range 0.1–300 GeV was

released in 2010 using only the first six months of its observation [54]. This included the discovery of 16 new gamma ray pulsars and confirmation of pulsed gamma ray emission from 24 known pulsars. Subsequently, 117 gamma ray pulsars with high-confidence detection at energies above 0.1 GeV were reported in the second *Fermi*-LAT pulsar catalog (2PC) using the first three years of data [55]. This sample of 117 gamma ray pulsars was divided into three classes: MSPs, young radio-loud and young radio-quiet pulsars. The more recent third *Fermi*-LAT pulsar catalog (3PC) identifies roughly 340 gamma ray pulsars using 12 years of data [52], which is approximately 10% of known pulsars. The increase in number of gamma ray pulsars detected by the *Fermi*-LAT so far is depicted in Figure 2. It is evident that the population of gamma ray pulsars has continued to grow after the launch of the *Fermi* satellite. The  $P - \dot{P}$  diagram of the gamma ray pulsars suggests that a large fraction of the *Fermi*-LAT detected pulsars can be identified as rotation-powered radio-loud MSPs [56]. Moreover, a significant fraction of these pulsars exhibit no emission in the radio band, hence the name radio-quiet pulsars. A comparative study of this relatively large population has led to new understanding of the emission process and geometry of the gamma ray pulsars [57]. The differential energy spectra of pulsars in the energy range 0.1–1 TeV, measured by the *Fermi*-LAT, are significantly curved and can be well fitted with a super-exponential cut-off power law of the form [58]

$$\frac{dN}{dE} = K \left( \frac{E}{E_0} \right)^{\frac{d}{b} - \Gamma_s} \exp \left[ \frac{d}{b^2} \left( 1 - \left( \frac{E}{E_0} \right)^b \right) \right] \quad (20)$$

where  $K$  is normalization (flux density at the reference energy  $E_0$ ),  $b$  and  $d$  are referred to as exponential index and spectral curvature, respectively, and  $\Gamma_s$  is the spectral slope.  $\Gamma_s$  and  $d$  are designated as spectral shape parameters.

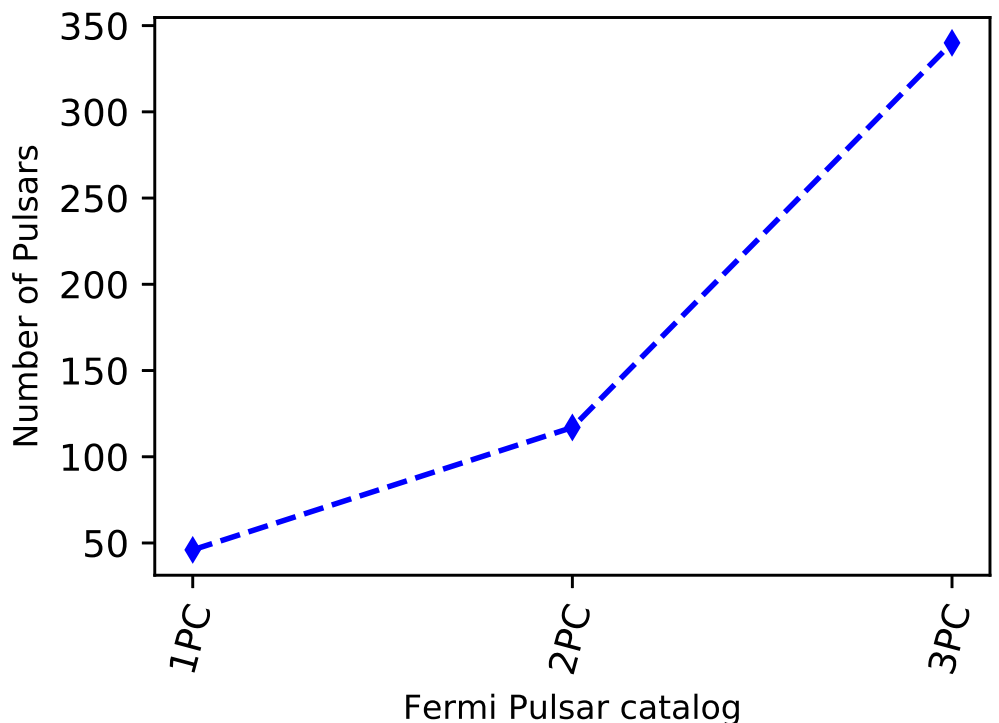


**Figure 2.** Evolution of number of gamma ray pulsars in the successive *Fermi*-LAT pulsar catalogs.

### 3.2. Gamma Ray Emission

The availability of good statistics and high-quality data on gamma ray pulsars over the last 50 years has provided a better perspective on the properties of their gamma ray emission. The primary radiative processes for bulk  $\gamma$  ray emission from pulsars are the

synchrotron-curvature radiation and inverse Compton scattering due to relativistic charged particles in the magnetosphere of neutron star. Therefore, the problem of high-energy emission from pulsars is two-fold: acceleration of charge particles to relativistic energies and radiative processes associated with the relativistic charge particles. According to the famous Goldreich–Julian model, the neutron star is considered to be a uniformly magnetized, perfectly conducting sphere with an internal magnetic field and an external dipole magnetic field [13]. The external magnetic field of the neutron star affects the pulsar magnetosphere, which is filled with ultra-relativistic electron–positron pairs and is assumed to be in ideal magnetohydrodynamic state or an ideal plasma with infinite conductivity. However, the exact structure and dynamics of pulsar magnetosphere are poorly understood. The charged particles at the surface of a neutron star experience a Lorentz force due to the neutron star's rotation. Since the neutron star is assumed to be a perfect conductor, the surface charges are redistributed so that the electric force counter balances the magnetic force, leading to a charge separation. The external electric field requires a continuous electric potential at the surface of the neutron star and the electric force on the surface charges greatly exceeds the gravitational attraction. This suggests that the accelerating electric field extracts particles from the surface of the neutron star and fills the magnetosphere. The number density of charge particles at the surface of neutron star is given by [13]

$$n_e = 7 \times 10^{-2} \frac{B_p}{P} \text{ cm}^{-3} \quad (21)$$

This simple model has several challenges, such as the problem of charge supply (considered only from the surface of neutron star), the question of return current or charge neutrality and its inherent instability despite many successes. Pair-production mechanisms, in the extreme environments of pulsars, are invoked to ensure the particle–photon cascades [59]. One photon-pair production ( $e^\pm$ -pair) may take place in the presence of a strong magnetic field ( $B$ ) if the following threshold condition is satisfied [60]

$$\left( \frac{E_\gamma}{m_e c^2} \right) \left( \frac{B}{1G} \right) \sin\theta \geq 10^{12.76} \quad (22)$$

where  $E_\gamma$  is the photon energy in units of  $m_e c^2$  and  $\theta$  is angle between direction of photon propagation and magnetic field. The collision between two high-energy photons may produce an  $e^\pm$ -pair in a region devoid of magnetic field if their energies satisfy the threshold condition [61]

$$E_{\gamma 1} E_{\gamma 2} = \frac{2(m_e c^2)^2}{(1 - \cos\theta)} \quad (23)$$

where  $E_{\gamma 1}$  and  $E_{\gamma 2}$  are energies of two photons undergoing collision and  $\theta$  is the angle between their momenta. The photon–photon collision may also lead to  $e^\pm$ -pair production in the presence of strong magnetic field provided that the  $e^\pm$ -pair has non-zero velocity to ensure the conservation of parallel momentum and energy.

An electric field is required to accelerate the charge particles along the neutron star magnetic field lines to explain the observed non-thermal high-energy radiation from pulsars. But the electric field, perpendicular to the magnetic field lines everywhere in the magnetosphere, implies no acceleration of charged particles. Geometrically, there exist several popular sites with a non-zero electric field component parallel to the magnetic field lines due to the breaking down of the ideal magnetohydrodynamic conditions in the pulsar magnetosphere. These privileged regions are considered as the accelerating and dissipative sites of the magnetospheric plasma, and their locations play an important role in the high-energy  $\gamma$  ray emission from pulsars, which is generally described by Equation (20).

The absence of plasma in *vacuum gaps* (often called accelerating gaps) provides three profound regions, namely, the Polar Cap, Outer Gap and Slot Gap with non-zero electric field for acceleration of charge particles in the pulsar magnetosphere. These scenarios are primarily based on the Goldreich–Julian model [13] for the case of an aligned rotator (a

neutron star with magnetic dipole moment along its rotation axis). The dipolar magnetic field lines inside the light cylinder (a boundary where an object co-rotating with the neutron star would need to move at the speed of light to maintain co-rotation) form closed loops or closed field lines. On the other hand, the magnetic field lines crossing the light cylinder are referred to as open field lines. Inside the light cylinder, particles move along the closed field lines and make the so-called co-rotating magnetosphere. The electric potential corresponding to each magnetic field line is associated with the latitude of the origin of field lines on the neutron star surface. For an aligned rotator, field lines that originate close to the equator (low latitude) correspond to very high electric potential. If these field lines are open, the positively charged particles tend to move along these lines and stream outward. The open field lines originating above the equator (high latitude) correspond to low electric potential. This causes negatively charged particles to move outward along the field lines. The charge density calculations in the magnetosphere suggest that it consists of separate conical regions of negatively and positively charged particles. With this brief description of the pulsar magnetosphere, different acceleration models (also known as *vacuum gap* models) are summarized below:

- **Polar Cap:** Historically, this is the first model considered for the acceleration of charge particles in the pulsar field by considering the case of an anti-aligned rotator (magnetic dipole vector and rotation vector are directly opposite each other) wherein the charge density and electric potential corresponding to the magnetic field lines are flipped. This causes the positively charged particles to move outward along the open field lines. A charge density depletion in the conical regions near the magnetic poles of the neutron star provides a large electric potential for acceleration of charge particles [62]. Particles are accelerated along the open field lines to altitudes where they attain high enough Lorentz factors to emit gamma ray photons. However, the strong magnetic field near the poles causes the absorption of high-energy gamma ray photons via magnetic pair-production. This leads to a gamma ray spectra of the form given by Equation (20) with a cut-off energy in the range 1–10 GeV. Therefore, this model is not able to explain gamma ray emission above 10 GeV from many pulsars detected by the *Fermi*-LAT [55].
- **Outer Gap:** This model is based on the case of an aligned rotator wherein positively charged particles move along the open field lines outside the light cylinder. This results in the creation of a gap, extending along the last closed field line up to the light cylinder. A charge density depletion leads to a large electric field component parallel to the magnetic field for accelerating the particles to relativistic energies required to emit high-energy gamma rays by the curvature emission [63]. These models require no polar cap pair-production and are invoked to explain the gamma ray spectra of most of the *Fermi*-LAT pulsars [55].
- **Slot Gap:** This scenario is assumed to lie between the polar cap and outer gap. The slot gap is considered as a narrow set of magnetic field lines near the boundary between open and closed field lines [64]. In this model, charged particles, originating from the neutron star surface, are accelerated from the polar cap along the last open field lines up to high altitudes (of the order of the radius of light cylinder). However, later works show that this model is not able to explain the observed gamma ray spectra of pulsars [65].

An alternative model to the above vacuum gap models is the *current sheet model*, where the acceleration of particles is attributed to the magnetic reconnection process [66]. This model is based on Monte Carlo simulations employing the Particle-In-Cell scheme of the plasma physics. It has now been firmly established that the magnetosphere of a non-aligned rotator entails a current sheet outside its light cylinder. The rotating distribution pattern of this current sheet moves at linear superluminal speed and emits the high-energy radiation [67]. This provides a reasonable explanation for non-thermal broadband radiation measured from pulsars with a phase lag between the radio and gamma ray peaks [68]. This model has, for the first time, provided an acceptable fit to the exceptionally broad

gamma ray spectrum of the well-known Crab pulsar [69]. Therefore, it is utterly important to detect high-energy gamma ray emission above  $\sim 20$  GeV from a large sample of pulsars to discriminate between different emission models. Pulsed emission above 50 GeV has been detected from a number of pulsars but only four very-high-energy gamma ray pulsars (Crab, Vela, Geminga, PSR B1706-44) have been detected in the GeV-TeV range by the ground-based state-of-the-art gamma ray telescopes. Thus, dedicated gamma ray monitoring of pulsars with low-energy threshold ground-based telescopes is one the main science drivers of very-high-energy gamma ray astronomy at present.

#### 4. MACE Telescope

The Major Atmospheric Cherenkov Experiment (MACE) is an extremely large state-of-the-art gamma ray telescope located at an altitude of  $\sim 4.3$  km at Hanle, Ladakh, India. The telescope was commissioned in September 2021 after its successful first light from the standard candle Crab Nebula in April 2021 [70]. Subsequently, various operating parameters of the telescope were optimized and tuned using a large number of engineering runs and repeated observations of the Crab Nebula. The telescope has been deployed for science data collection for more than one year. During this period, it has successfully detected high-energy gamma ray photons from a number of candidate sources, including the recent giant flaring episode of the radio galaxy NGC 1275 in December 2022 and January 2023 [71,72]. The MACE telescope is designed to cover the high-energy gamma ray band above 20 GeV with a point source sensitivity better than the existing stand-alone imaging atmospheric Cherenkov telescopes (IACTs) in the world [73,74]. At present, the telescope is capable of detecting high-energy gamma ray photons from the Crab Nebula with a sensitivity of  $5\sigma$  in a few minutes (internal communication) in the energy range above 50 GeV. A picture of the MACE telescope at Hanle is shown in Figure 3. It is equipped with a big quasi-parabolic light reflector of 21 m diameter and 25 m focal length. This offers a total light collection area of  $\sim 340$  m $^2$ . Such a large area is achieved by using a tessellated structure comprising 356 mirror panels of size 0.986 m  $\times$  0.986 m each. Each panel consists of four square-shaped spherical metallic mirror facets of size 0.488 m  $\times$  0.488 m each [75], with similar focal length. The reflecting surface of the mirror facets, coated with a protection layer of SiO<sub>2</sub> of thickness  $\sim 120$  nm, has an average reflectance of  $\sim 85\%$ . An active mirror alignment control system employing linear actuators and diode lasers fitted on each panel is used to obtain the best possible parabolic approximation and optimum focusing in all orientations of the basket. An imaging camera at the focal plane has an optical field of view of  $4.36^\circ \times 4.03^\circ$  and a uniform pixel resolution of  $0.125^\circ$ . It consists of 1088 photomultiplier tubes (PMTs) with high quantum efficiency (above 30%) and medium gain ( $\sim 10^4$ ). The MACE camera is a custom-designed, event-driven system with state-of-the-art technologies for in-house signal processing electronics and high-speed data acquisition. The entire telescope structure is supported by an altitude-azimuth drive system. With the telescope's moving weight of 180 ton, the drive system enables the pointing and tracking of a gamma ray source with an accuracy of  $\sim 1$  arcmin in the presence of wind blowing at a speed of up to 45 km/h. A data archival storage system with a capacity of 80 TB is housed in the control room at the telescope site for safe and secure storage of the MACE data as a large data volume of  $\sim 50$  GB is generated during every hour of observation.

The combination of the large light collector of the telescope and the high altitude of the site offers a unique opportunity to achieve a low gamma ray energy threshold close to  $\sim 20$  GeV. It helps in exploring the gamma ray Universe beyond a redshift  $z \geq 2$  [76]. It belongs to the class of extremely large IACTs (e.g., MAGIC-I, HESS-II and LST-1) operating in the world. The threshold energy of MACE is similar to that of HESS-II and LST-1. In the energy range above 20–150 GeV, the point source sensitivity ( $\sim 10^{-11}$  ph cm $^{-2}$  s $^{-1}$ ) of MACE is expected to be better than that of MAGIC-I [73,74]. However, beyond 150 GeV, MACE sensitivity ( $\sim 10^{-10}$  ph cm $^{-2}$  s $^{-1}$ ) is slightly lower than MAGIC-I. Therefore, the low threshold energy and very high point source sensitivity of MACE make it an ideal instrument for the observation of gamma ray pulsars detected by the *Fermi*-LAT. Moreover,

the geographical location (the easternmost) of MACE appropriately fills the longitudinal gap between different major IACTs of its class around the globe. It has the distinction of being the highest-altitude existing IACT in the world. Owing to its unique features, the MACE telescope will play an important role in the study of gamma ray sources like pulsars in the energy range 20–100 GeV, which remains unexplored by ground-based telescopes.



**Figure 3.** MACE gamma ray telescope at Hanle, Ladakh, India.

### 5. Pulsars with MACE

The gamma ray spectra of most of the pulsars observed by the *Fermi*-LAT have a cut-off energy in the range 1–10 GeV. Due to this, the gamma ray flux at higher energy end of the spectrum decreases very quickly. Therefore, ground-based telescopes with better sensitivity than the *Fermi*-LAT in the energy range above 50 GeV play a crucial role in determining the pulsar spectra in the very-high-energy band. With this motivation, we have developed a formalism based on the following arguments to select a sample of the *Fermi*-LAT pulsars for their observation with the MACE telescope.

In general, pulsar light curves or phasograms exhibit a two-peak structure. The first peak position at phase  $P_1$  is attributed to the radio emission and is therefore referred to as the main pulse. This is assigned zero phase, and the position of the second peak at phase  $P_2$  is calculated with respect to  $P_1$ . However, there exist pulsars like Geminga, which have only one peak in their phasogram. The pulse amplitude corresponding to these peaks changes with the energy and the  $P_2$  peak is observed to dominate with increasing energy. Therefore, the observation of pulsars in the very-high-energy range by ground-based telescopes like MACE is governed by the detection of pulse at  $P_2$  at  $5\sigma$  confidence level in their phasogram over the huge isotropic cosmic ray background mainly due to protons. Thus, if a gamma ray pulsar is residing within the nebula, both gamma rays from the nebula and cosmic ray protons will act as the background for pulsar detection with ground-based telescopes. These background events lack in periodicity and, hence, have no phase, whereas photons originating from the pulsars have a well-defined phase associated with their rotation. Thus, the background events are uniformly distributed in the light curve or phasogram of a pulsar, and the gamma ray signal from a pulsar will pile up in a particular phase-bin. If  $N_{bins}$  is the number of bins in the phasogram of a pulsar, then the background will be reduced by a factor of  $N_{bins}$ . For  $N_{bins} = 30$ , the observation time

required for detection of dominant gamma ray peak ( $T_P$ ) in the phasogram of a pulsar at  $5\sigma$  statistical significance level with the MACE telescope is estimated as

$$T_P \text{ (hours)} = 0.025 \times \left( \frac{1.66 \times 10^{-9}}{I_P} \right)^2 \quad (24)$$

where  $I_P$  is the integral flux of dominating peak above 30 GeV in units of  $\text{ph cm}^{-2} \text{s}^{-1}$ . We apply this methodology to two well-known gamma ray pulsars Crab and Geminga to estimate the expected time for MACE observations as their gamma ray spectra are available in the energy range covered by the MACE telescope.

### 5.1. Crab Pulsar

The Crab pulsar (PSR J0534+2200) is the most studied pulsar in all energy bands, from radio to TeV, and is also the first pulsar detected by any ground-based gamma ray telescope. It is a normal pulsar with  $P = 33$  ms and  $\dot{P} = 4.2 \times 10^{-13} \text{ s s}^{-1}$ . After many attempts, the MAGIC-I telescope detected pulsed emission above 25 GeV from Crab in 2008 and revealed the presence of high cut-off energy in the gamma ray spectrum [77]. Subsequently, the VERITAS collaboration reported pulsed emission from Crab in the energy range 100–400 GeV [78]. Long-term observations of the Crab pulsar with the MAGIC telescopes resulted in the first ever detection of very -high-energy gamma ray emission in the energy range 70 GeV–1.5 TeV [79]. This finding strongly supported the inverse-Compton origin of the gamma ray photons from the Crab pulsar. It is among the few pulsars that have been detected across the entire electromagnetic spectrum from radio up to gamma rays of beyond 1 TeV [79]. Its emission profile has three components: two dominant pulses separated by 0.4 in phase, observed from radio to TeV gamma rays, and a third bridge component. The main pulse corresponding to  $P_1$  at phase 0 dominates at radio frequencies. The second pulse corresponding to  $P_2$  at phase 0.4 (also referred to as interpulse) is weaker at radio frequencies and becomes dominant at very-high-energy gamma rays. The bridge component (defined as the pulse phase between the main pulse and the second pulse) is observed in gamma rays up to 150 GeV [79]. The stereoscopic MAGIC telescope has detected a signal at  $6.6\sigma$  and  $8.8\sigma$  for  $P_1$  and  $P_2$ , respectively, in 152 h of crab pulsar observations at zenith angles below  $35^\circ$ . The differential energy spectra of gamma ray photons corresponding to  $P_1$  and  $P_2$  are described by a power law in the range 70 GeV to 1.5 TeV. The  $P_2$  spectrum is relatively hard and the corresponding integral flux is two times that of  $P_1$ . For  $I_P = I_{P2} = 3.35 \times 10^{-11} \text{ ph cm}^{-2} \text{s}^{-1}$ , the corresponding detection time for MACE is estimated to be  $T_P \sim 61.38$  h using Equation (24).

### 5.2. Vela

The Vela pulsar (PSR J0835-4510) with  $P = 89.3$  ms and  $\dot{P} = 1.2 \times 10^{-13} \text{ s s}^{-1}$  is the second gamma ray pulsar detected, after Crab. It is located in the southern hemisphere at a distance of 280 pc from Earth. The light curve of the Vela pulsar exhibits two peaks,  $P_1$  and  $P_2$ , separated by a phase of 0.43. The two peaks are connected by a bridge emission labeled as  $P_3$ . The largest IACT, HESS-II, made the first ground-based detection of pulsed gamma ray emission in the energy range of sub-20 GeV to 100 GeV from the Vela pulsar [80]. The gamma ray signal was detected at the  $P_2$  peak with a statistical significance level of more than  $15\sigma$ . The power-law model with a very soft spectral index ( $\Gamma_s \sim 4.1$ ) very well describes the differential energy spectrum of the  $P_2$  peak in the energy range 10–100 GeV. Being located in the southern hemisphere, the Vela pulsar will be visible to the MACE telescope only at large zenith angles above  $75^\circ$ . At these zenith angles, the threshold energy for MACE may increase beyond 150 GeV. Therefore, we have not considered this source as potential candidate for MACE observations in the present work.

### 5.3. Geminga

The Geminga pulsar (PSR J0633+1746) is a radio-quiet gamma ray pulsar with  $P = 237$  ms and  $\dot{P} = 1.1 \times 10^{-14}$  s s $^{-1}$ . Located at a distance of 250 pc from Earth, it is one of the closest gamma ray pulsars. The MAGIC telescope has detected a pulsed gamma ray signal from Geminga at  $6.3\sigma$  statistical significance level in 80 h of observations [81]. Only the  $P_2$  peak is observed to be dominant in the phasogram in the energy range of 15–75 GeV. The corresponding integral flux is estimated as  $I_P = I_{P2} = 2.18 \times 10^{-11}$  ph cm $^{-2}$  s $^{-1}$ . For this flux level, the total observation time required for MACE observations in the energy range 30 GeV–5 TeV is calculated to be  $T_P \sim 144$  h.

### 5.4. Pulsar Catalog for MACE

As discussed in Section 3.1, the current population of gamma ray pulsars detected by the *Fermi*-LAT is  $\sim 340$ . The distribution of integral energy flux in the energy range 0.1–100 GeV for all the *Fermi*-LAT pulsars is shown in Figure 4. It is observed that majority of the pulsars have high-energy flux  $\sim 1.4 \times 10^{-11}$  erg cm $^{-2}$  s $^{-1}$ , which is typically two order less than the corresponding Crab pulsar flux. The *Fermi*-LAT spectra of most of the pulsars are described by Equation (20). The cut-off energy can be approximately calculated as

$$E_c = E_0 \times \left( \frac{b^2}{d} \right)^{\frac{1}{b}} \quad (25)$$

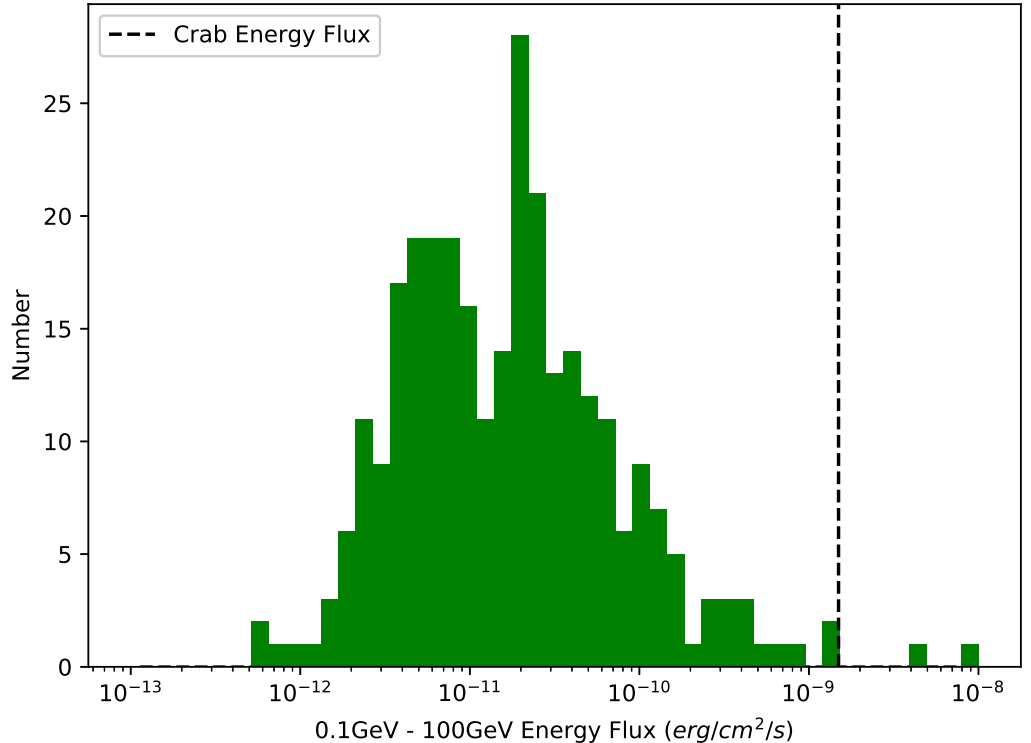


**Figure 4.** Histogram of energy flux of the *Fermi*-LAT pulsars in the energy range 0.1–100 GeV.

The distribution of the cut-off energy ( $E_c$ ) for all the *Fermi*-LAT pulsars is reported in Figure 5. It is found that most of the pulsars have a cut-off energy close to 0.8 GeV, whereas only 33 pulsars have  $E_c \geq 2$  GeV.

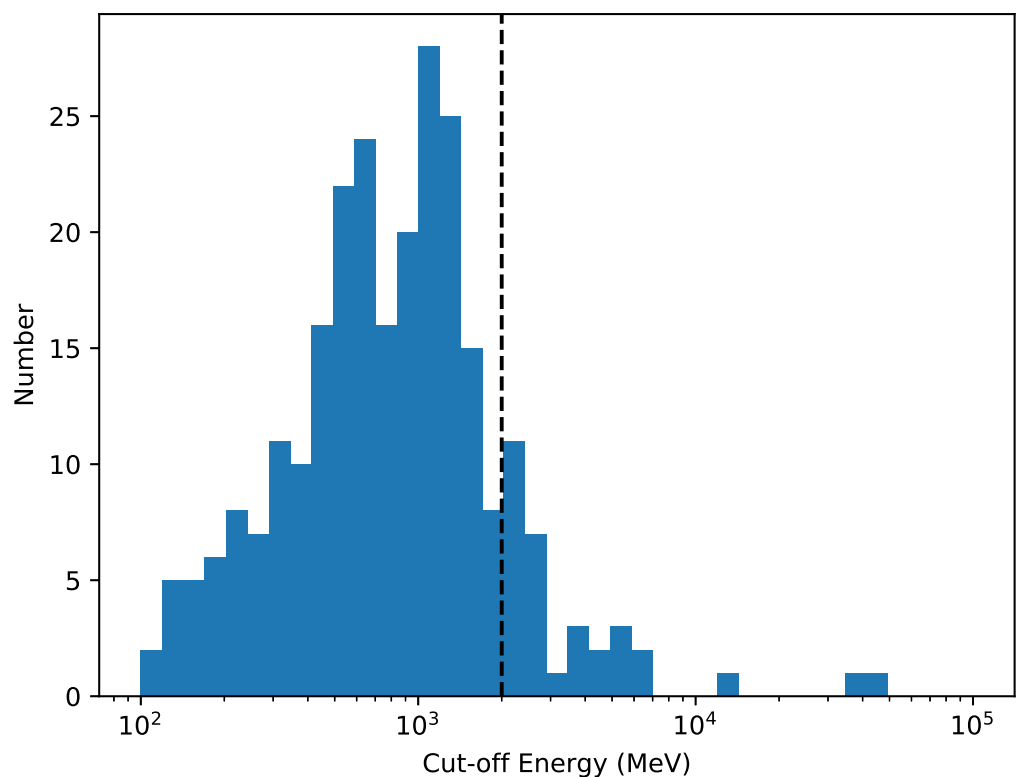


**Figure 5.** Histogram of the cut-off energy of the Fermi-LAT pulsars. The vertical dotted line indicates  $E_c = 2$  GeV.

Applying the visibility criteria of the astrophysical sources from a given observatory, only 96 *Fermi*-LAT pulsars are found to be visible from the MACE site at Hanle ( $32.8^\circ$  N,  $78.9^\circ$  E). The next criterion is the identification of pulsars which have  $E_c \geq 2$  GeV. This constraint further reduces the number of pulsars from 96 to 8. Lastly, we check for the significance of pulsation in the energy range 10–30 GeV, overlapping with MACE, to be more than  $2\sigma$ . Based on the above criterion, we are left with only six pulsar candidates (other than Crab and Geminga) from the 4FGL-DR3 catalog for MACE observations. A summary of these sources is given in the Table 1.

**Table 1.** List of gamma ray pulsar candidates derived from the 4FGL-DR3 catalog for observations with the MACE telescope.

Sr. No.	Name	$P$ (s)	$\dot{P}$	$E_c$ (GeV)	Significance (10–30 GeV)
1	J1807.1+2822	0.015084	$3.75 \times 10^{-20}$	6.434	$2.17\sigma$
2	J1908.9+2103	0.002564	$1.38 \times 10^{-20}$	2.063	$4.26\sigma$
3	J1913.3+1019	0.035909	$3.36 \times 10^{-15}$	37.886	$7.23\sigma$
4	J2047.3+1051	0.004290	$2.1 \times 10^{-20}$	2.722	$3.52\sigma$
5	J2052.7+1218	0.001985	$6.7 \times 10^{-21}$	3.595	$3.18\sigma$
6	J2302.7+4443	0.005192	$1.38 \times 10^{-20}$	2.077	$12.64\sigma$

## 6. Summary and Outlook

Gamma ray pulsars represent a dominant population of Galactic sources in the Universe. However, emission of very-high-energy gamma ray photons from pulsars remains a fundamental problem in astrophysics even after more than 50 years of discovery. Individual pulsars of the *Fermi*-LAT catalog have not been observed so far by the ground-based telescopes, except a few which have exhibited giant pulses, such as Crab, Geminga and Vela. In this work, we have briefly reviewed the different aspects of the gamma ray pulsars and outline the importance of the recently commissioned MACE telescope in this field.

A total of six pulsars, other than very-high-energy gamma ray pulsars Crab and Geminga, have been identified as probable candidates for MACE observations in upcoming times.

**Author Contributions:** A.P., conceptualization, data curation and original draft preparation; K.K.S., conceptualization and original draft preparation; K.K.Y., review and editing. All authors have read and agreed to the published version of the manuscript.

**Funding:** This research received no external funding.

**Acknowledgments:** The authors thank the three anonymous reviewers and the academic editor for their critical comments and suggestions.

**Conflicts of Interest:** The authors declare no conflict of interest.

## Notes

- 1 <https://www.atnf.csiro.au/research/pulsar/psrcat/> (accessed on 20 January 2023)

## References

1. Janka, H.-T.; Langanke, K.; Marek, A.; Martínez-Pinedo, G.; Müller, B. Theory of core-collapse supernovae. *Phys. Rep.* **2007**, *442*, 38–74. [[CrossRef](#)]
2. Shapiro, S.L.; Teukolsky, S.A. *Black Holes, White Dwarfs, and Neutron Stars: The Physics of Compact Objects*; John Wiley & Sons: Hoboken, NJ, USA, 1983.
3. Miller, M.C.; Miller, J.M. The masses and spins of neutron stars and stellar-mass black holes. *Phys. Rep.* **2015**, *548*, 1–34. [[CrossRef](#)]
4. Singh, K.K.; Meintjes, P.J.; Yadav, K.K. Properties of white dwarf in the binary system AR Scorpii and its observed features. *Mod. Phys. Lett. A* **2021**, *36*, 2150096. [[CrossRef](#)]
5. Woosley, S.E.; Heger, A.; Weaver, T.A. The evolution and explosion of massive stars. *Rev. Mod. Phys.* **2002**, *74*, 1015–1071. [[CrossRef](#)]
6. Müller, B. Hydrodynamics of core-collapse supernovae and their progenitors. *Living Rev. Comput. Astrophys.* **2020**, *6*, 3. [[CrossRef](#)]
7. Spruit, H.; Phinney, E.S. Birth kicks as the origin of pulsar rotation. *Nature* **1998**, *393*, 139–141. [[CrossRef](#)]
8. Janka, H.-T.; Wongwathanarat, A.; Kramer, M. Supernova Fallback as Origin of Neutron Star Spins and Spin-kick Alignment. *Astrophys. J.* **2022**, *926*, 9. [[CrossRef](#)]
9. Coleman, M.S.B.; Burrows, A. Kicks and induced spins of neutron stars at birth. *Mon. Not. R. Astron. Soc.* **2022**, *517*, 3938–3961. [[CrossRef](#)]
10. Hewish, A.; Bell, S.J.; Pilkington, J.D.H.; Scott, P.F.; Collins, R.A. Observation of a rapidly pulsating radio source. *Nature* **1968**, *217*, 709. [[CrossRef](#)]
11. Gold, T. Rotating neutron stars as the origin of the pulsating radio sources. *Nature* **1968**, *218*, 731. [[CrossRef](#)]
12. Spitkovsky, A. Time-dependent Force-free Pulsar Magnetospheres: Axisymmetric and Oblique Rotators. *Astrophys. J. Lett.* **2006**, *648*, L51–L54. [[CrossRef](#)]
13. Goldreich, P.; Julian, W.H. Pulsar Electrodynamics. *Astron. J.* **1969**, *157*, 869. [[CrossRef](#)]
14. Arons, J.; Tavani, M. Relativistic Particle Acceleration in Plerions. *Astrophys. J. Suppl. Ser.* **1994**, *90*, 797. [[CrossRef](#)]
15. Radhakrishnan, V.; Manchester, R.N. Detection of a Change of State in the Pulsar PSR 0833-45. *Nature* **1969**, *222*, 228. [[CrossRef](#)]
16. Reichley, P.E.; Downs, G.S. Observed Decrease in the Periods of Pulsar PSR 0833-45. *Nature* **1969**, *222*, 229. [[CrossRef](#)]
17. Hulse, R.A.; Taylor, J.H. Discovery of a pulsar in a binary system. *Astrophys. J. Lett.* **1975**, *195*, L51–L53. [[CrossRef](#)]
18. Backer, D.C.; Kulkarni, S.R.; Heiles, C.; Davis, M.M.; Goss, W.M. A millisecond pulsar. *Nature* **1982**, *300*, 615–618. [[CrossRef](#)]
19. Burgay, M.; D’Amico, N.; Possenti, A.; Manchester, R.N.; Lyne, A.G.; Joshi, B.C.; McLaughlin, M.A.; Kramer, M.; Sarkissian, J.M.; Camilo, F.; et al. An increased estimate of the merger rate of double neutron stars from observations of a highly relativistic system. *Nature* **2003**, *426*, 531–533. [[CrossRef](#)]
20. Manchester, R.N.; Hobbs, G.B.; Teoh, A.; Hobbs, M. The Australia Telescope National Facility Pulsar Catalogue. *Astron. J.* **2005**, *129*, 1993–2006. [[CrossRef](#)]
21. Terzić, T.; Kerszberg, D.; Strišović, J. Probing Quantum Gravity with Imaging Atmospheric Cherenkov Telescopes. *Universe* **2021**, *7*, 345. [[CrossRef](#)]
22. Bhattacharya, D.; Van den Heuvel, E.P.J. Formation and evolution of binary and millisecond radio pulsars. *Phys. Rep.* **1991**, *203*, 1–124. [[CrossRef](#)]
23. Poutanen, J. Accretion-powered millisecond pulsars. *Adv. Spac. Res.* **2006**, *38*, 2697–2703. [[CrossRef](#)]
24. Wijnands, R.; van der Klis, M. A millisecond pulsar in an X-ray binary system. *Nature* **1998**, *394*, 344–346. [[CrossRef](#)]
25. Archibald, A.M.; Stairs, I.H.; Ransom, S.M.; Kaspi, V.M.; Kondratiev, V.I.; Lorimer, D.R.; McLaughlin, M.A.; Boyles, J.; Hessels, J.W.; Lynch, R.; et al. A Radio Pulsar/X-ray Binary Link. *Science* **2009**, *324*, 1411–1414. [[CrossRef](#)] [[PubMed](#)]
26. Konar, S.; Bagchi, M.; Bandyopadhyay, D.; Banik, S.; Bhattacharya, D.; Bhattacharyya, S.; Gangadhara, R.T.; Gopakumar, A.; Gupta, Y.; Joshi, B.C.; et al. Neutron Star Physics in the Square Kilometre Array Era: An Indian Perspective. *J. Astrophys. Astron.* **2016**, *37*, 36. [[CrossRef](#)]

27. Tauris, T.M. Five and a Half Roads to Form a Millisecond Pulsar. *Astron. Soc. Pac. Conf. Ser.* **2011**, *447*, 285.
28. Bhattacharyya, S. Measurement of neutron star parameters: A review of methods for low-mass X-ray binaries. *Adv. Spac. Res.* **2010**, *45*, 949–978. [[CrossRef](#)]
29. Caballero, I.; Wilms, J. X-ray pulsars: A review. *Mem. Soc. Astron. Ital.* **2012**, *83*, 230.
30. Kaspi, V.M. Grand unification of neutron stars. *Proc. Natl. Acad. Sci. USA* **2010**, *107*, 7147–7152. [[CrossRef](#)] [[PubMed](#)]
31. Thompson, C.; Duncan, R.C. The Soft Gamma Repeaters as Very Strongly Magnetized Neutron Stars. II. Quiescent Neutrino, X-ray, and Alfvén Wave Emission. *Astrophys. J.* **1996**, *473*, 322. [[CrossRef](#)]
32. Lorimer, D.R. Binary and Millisecond Pulsars. *Living Rev. Relativ.* **2008**, *11*, 8. [[CrossRef](#)] [[PubMed](#)]
33. Baring, M.G. High-energy emission from pulsars: The polar cap scenario. *Adv. Spac. Res.* **2004**, *33*, 552–560. [[CrossRef](#)]
34. Harding, A.K.; Stern, J.V.; Dyks, J.; Frackowiak, M. High-Altitude Emission from Pulsar Slot Gaps: The Crab Pulsar. *Astrophys. J.* **2008**, *680*, 1378–1393. [[CrossRef](#)]
35. Igoshev, A.P.; Popov, S.B.; Hollerbach, R. Evolution of Neutron Star Magnetic Fields. *Universe* **2021**, *7*, 351. [[CrossRef](#)]
36. Tauris, T.M.; Manchester, R.N. On the Evolution of Pulsar Beams. *Mon. Not. R. Astron. Soc.* **1998**, *298*, 625–636. [[CrossRef](#)]
37. Haskell, B.; Melatos, A. Models of pulsar glitches. *Int. J. Mod. Phys. D* **2015**, *24*, 1530008. [[CrossRef](#)]
38. Manchester, R.N. Pulsar timing and its applications. *J. Phys. Conf. Ser.* **2017**, *932*, 012002. [[CrossRef](#)]
39. Damour, T.; Taylor, J.H. Strong-field tests of relativistic gravity and binary pulsars. *Phys. Rev. D* **1992**, *45*, 1840–1868. [[CrossRef](#)]
40. Hobbs, G. Developing a Pulsar-Based Time Standard. *Highlights Astron.* **2015**, *16*, 207–208. [[CrossRef](#)]
41. Pétri, J. Pulsar gamma-ray emission in the radiation reaction regime. *Mon. Not. R. Astron. Soc.* **2019**, *484*, 5669–5691. [[CrossRef](#)]
42. Igoshev, A.P.; Popov, S.B. Braking indices of young radio pulsars: Theoretical perspective. *Mon. Not. R. Astron. Soc.* **2020**, *499*, 2826–2835. [[CrossRef](#)]
43. Lyne, A.G.; Jordan, C.; Graham-Smith, F.; Espinoza, C.; Stappers, B.; Weltrvrede, P. 45 years of rotation of the Crab pulsar. *Mon. Not. R. Astron. Soc.* **2015**, *446*, 857–864. [[CrossRef](#)]
44. Mitra, A.; Singh, K.K. Thermal Radiation from Compact Objects in Curved Space-Time. *Universe* **2022**, *8*, 504. [[CrossRef](#)]
45. Browning, R.; Ramsden, D.; Wright, P.J. Detection of Pulsed Gamma Radiation from the Crab Nebula. *Nat. Phys. Sci.* **1971**, *232*, 99–101. [[CrossRef](#)]
46. Kniffen, D.A.; Hartman, R.C.; Thompson, D.J.; Bignami, G.F.; Fichtel, C.E. Gamma radiation from the Crab Nebula above 35 MeV. *Nature* **1974**, *251*, 397–399. [[CrossRef](#)]
47. Thompson, D.J.; Fichtel, C.E.; Kniffen, D.A.; Ogelman, H.B. SAS-2 high-energy gamma-ray observations of the Vela pulsar. *Astrophys. J. Lett.* **1975**, *200*, L79–L82. [[CrossRef](#)]
48. Swanenburg, B.N.; Bennett, K.; Bignami, G.F.; Buccheri, R.; Caraveo, P.; Hermsen, W.; Kanbach, G.; Lichti, G.G.; Masnou, J.L.; Mayer-Hasselwander, H.A.; et al. Second COS-B catalogue of high-energy gamma-ray sources. *Astrophys. J. Lett.* **1981**, *243*, L69–L73. [[CrossRef](#)]
49. Bertsch, D.L.; Brazier, K.T.S.; Fichtel, C.E.; Hartman, R.C.; Hunter, S.D.; Kanbach, G.; Kniffen, D.A.; Kwok, P.W.; Lin, Y.C.; Mattox, J.R.; et al. Pulsed high-energy  $\gamma$ -radiation from Geminga (1E0630+178). *Nature* **1992**, *357*, 306–307. [[CrossRef](#)]
50. Bignami, G.F.; Caraveo, P.A. Geminga: Its Phenomenology, Its Fraternity, and Its Physics. *Ann. Rev. Astron. Astrophys.* **1996**, *34*, 331–382. [[CrossRef](#)]
51. Caraveo, P.A. Gamma-Ray Pulsar Revolution. *Ann. Rev. Astron. Astrophys.* **2014**, *52*, 221–250. [[CrossRef](#)]
52. Smith, D.A.; Bruel, P.; Clark, C.J.; Guillemot, L.; Kerr, M.T.; Ray, P.; Abdollahi, S.; Ajello, M.; Baldini, L.; Ballet, J.; et al. The Third Fermi Large Area Telescope Catalog of Gamma-ray Pulsars. *arXiv* **2023**, arXiv:2307.11132.
53. Fermi-LAT Collaboration. The Large Area Telescope on the Fermi Gamma-Ray Space Telescope Mission. *Astrophys. J.* **2009**, *697*, 1071–1102. [[CrossRef](#)]
54. Fermi-LAT Collaboration. The First Fermi Large Area Telescope Catalog of Gamma-ray Pulsars. *Astrophys. J. Suppl. Ser.* **2010**, *187*, 460–494. [[CrossRef](#)]
55. Fermi-LAT Collaboration. The Second Fermi Large Area Telescope Catalog of Gamma-Ray Pulsars. *Astrophys. J. Suppl. Ser.* **2013**, *208*, 17. [[CrossRef](#)]
56. Limyansky, B. The Third Fermi Pulsar Catalog. *Am. Astron. Soc.* **2019**, *17*, 109.
57. Harding, A.K. The neutron star zoo. *Front. Phys.* **2013**, *8*, 679–692. [[CrossRef](#)]
58. Fermi-LAT Collaboration. Incremental Fermi Large Area Telescope Fourth Source Catalog. *Astrophys. J. Suppl. Ser.* **2022**, *260*, 53. [[CrossRef](#)]
59. Daugherty, J.K.; Harding, A.K. Electromagnetic cascades in pulsars. *Astrophys. J.* **1982**, *252*, 337. [[CrossRef](#)]
60. Sturrock, P.A. A Model of Pulsars. *Astrophys. J.* **1971**, *164*, 529. [[CrossRef](#)]
61. Gould, R.J.; Schréder, G. Opacity of the Universe to High-Energy Photons. *Phys. Rev. Lett.* **1966**, *16*, 252–254. [[CrossRef](#)]
62. Ruderman, M.A.; Sutherland, P.G. Theory of pulsars: Polar gaps, sparks, and coherent microwave radiation. *Astrophys. J.* **1975**, *196*, 51–72. [[CrossRef](#)]
63. Cheng, K.S.; Ho, C.; Ruderman, M. Energetic Radiation from Rapidly Spinning Pulsars. I. Outer Magnetosphere Gaps. *Astrophys. J.* **1986**, *300*, 500. [[CrossRef](#)]
64. Arons, J. Pair creation above pulsar polar caps: Geometrical structure and energetics of slot gaps. *Astrophys. J.* **1983**, *266*, 215–241. [[CrossRef](#)]

65. Hirotani, K. Outer-Gap versus Slot-Gap Models for Pulsar High-Energy Emissions: The Case of the Crab Pulsar. *Astrophys. J. Lett.* **2008**, *688*, L25. [[CrossRef](#)]
66. Dmitri, A.U.; Anatoly, S. Physical Conditions in the Reconnection Layer in Pulsar Magnetospheres. *Astrophys. J.* **2014**, *780*, 3.
67. Philippov, A.; Kramer, M. Pulsar Magnetospheres and Their Radiation. *Ann. Rev. Astron. Astrophys.* **2022**, *60*, 495–558. [[CrossRef](#)]
68. Ardavan, H. Radiation by the superluminally moving current sheet in the magnetosphere of a neutron star. *Mon. Not. R. Astron. Soc.* **2021**, *507*, 4530–4563. [[CrossRef](#)]
69. Ardavan, H. Congruity of the Crab Pulsar’s  $\gamma$ -ray spectrum with the spectral distribution of tightly focused caustics. *Astron. Astrophys.* **2023**, *672*, A154. [[CrossRef](#)]
70. Yadav, K.K.; Chouhan, N.; Thubstan, R.; Norlha, S.; Hariharan, J.; Borwankar, C.; Chandra, P.; Dhar, V.K.; Mankuzhyil, N.; Godambe, S.; et al. Commissioning of the MACE gamma-ray telescope at Hanle, Ladakh, India. *Curr. Sci.* **2022**, *123*, 1428–1435. [[CrossRef](#)]
71. Yadav, K.K. MACE detection of very high energy gamma-ray flare from the radio galaxy NGC 1275. *Astron. Telegr.* **2022**, 15823 .
72. Yadav, K.K. Detection of Renewed Gamma-Ray Flare from the Radio Galaxy NGC 1275 with the MACE telescope. *Astron. Telegr.* **2023**, 15856, 1.
73. Singh, K.K.; Yadav, K.K. 20 Years of Indian Gamma Ray Astronomy Using Imaging Cherenkov Telescopes and Road Ahead. *Universe* **2021**, *7*, 96. [[CrossRef](#)]
74. Singh, K.K. Gamma-ray astronomy with the imaging atmospheric Cherenkov telescopes in India. *J. Astrophys. Astron.* **2022**, *43*, 3. [[CrossRef](#)]
75. Dhar, V.K.; Singh, K.K.; Venugopal, K.; Yadav, K.K.; Koul, R.; Balasubramaniam, R. Development of a new type of metallic mirrors for 21 meter MACE  $\gamma$ -ray telescope. *J. Astrophys. Astron.* **2022**, *43*, 17. [[CrossRef](#)]
76. Tolamatti, A.; Singh, K.K.; Yadav, K.K. Feasibility study of observing  $\gamma$ -ray emission from high redshift blazars using the MACE telescope. *J. Astrophys. Astron.* **2022**, *43*, 49. [[CrossRef](#)]
77. MAGIC Collaboration. Observation of Pulsed  $\gamma$ -Rays Above 25 GeV from the Crab Pulsar with MAGIC. *Science* **2008**, *322*, 1221–1224. [[CrossRef](#)]
78. VERITAS Collaboration. Detection of Pulsed Gamma Rays Above 100 GeV from the Crab Pulsar. *Science* **2011**, *334*, 69. [[CrossRef](#)]
79. MAGIC Collaboration. Teraelectronvolt pulsed emission from the Crab Pulsar detected by MAGIC. *Astron. Astrophys.* **2016**, *585*, A133. [[CrossRef](#)]
80. H.E.S.S. Collaboration. First ground-based measurement of sub-20 GeV to 100 GeV  $\gamma$ -Rays from the Vela pulsar with H.E.S.S. II. *Astron. Astrophys.* **2018**, *620*, A66. [[CrossRef](#)]
81. MAGIC Collaboration. Detection of the Geminga pulsar with MAGIC hints at a power-law tail emission beyond 15 GeV. *Astron. Astrophys.* **2020**, *643*, L14. [[CrossRef](#)]

**Disclaimer/Publisher’s Note:** The statements, opinions and data contained in all publications are solely those of the individual author(s) and contributor(s) and not of MDPI and/or the editor(s). MDPI and/or the editor(s) disclaim responsibility for any injury to people or property resulting from any ideas, methods, instructions or products referred to in the content.